TÜBİTAK

Influence of silicon dioxide medium on the structural and electrical properties of nickel zinc ferrite

Jacob GEORGE[1,*], **Abraham Kutticheril EAPEN**[2]

[1]Department of Physics, Faculty of Science, Government College Kottayam, Kottayam, Kerala, India
[2]Department of Physics, Faculty of Science, St. Berchamans College, Changanacherry, Kottayam, Kerala, India

Abstract: Nickel zinc ferrite $[(Ni_{0.65} Zn_{0.35} Fe_2 O_4)_x / (SiO_2)_{1-x}$ where, x = 1.0, 0.85, 0.65, 0.50, 0.35, and 0.15] is synthesized using the glyoxylate precursor method. The synthesis, characterization, and electrical study of nickel zinc ferrites/SiO_2 powder with low dielectric constant, very low conductivity, and loss tangent with low frequency dispersion, suitable for good insulators, is reported here. X-ray diffraction, TGA, and FT-IR studies are employed for identifying crystalline phases and structure. Crystallite size is calculated by the Scherrer formula and Williamson–Hall equation and found to fall in the range of 4.9–25 nm. TEM of the samples shows spherical particles of uniform size distribution and the spotty rings of SAED patterns are analyzed for identifying the crystal planes. The study confirms a simple and efficient way to synthesize single-phase nickel zinc ferrite (NZFO) spherical particles of nano size ($\approx$15 nm at 1000 °C) with lower particle agglomeration in comparison to any other methods. Electrical studies are carried out using an LCR meter. The observed value of dielectric constant falls in the range of 10–80, loss tangent in the range of 0.05–0.4, and electrical conductivity in the range of 10^{-4} to 10^{-7} mho m^{-1}. These values are respectively functions of temperature, frequency, and the ferrite content in ferrite/SiO_2 samples. A proper selection of ferrite concentration in the silica medium enables one to prepare NZFO/SiO_2 material of very low loss tangent with dielectric constant in the range of 10–80.

Key words: Nickel zinc ferrite, ethylene glycol, tetraethyl orthosilicate, dielectric constant, dielectric conductivity, loss tangent

1. Introduction

Ferrites belong to an important class of spinel structured materials having the chemical formula $AB_2 O_4$, where A and B are divalent and trivalent cations Ni, Zn, Mn, Mg, Cr, Co, Fe, etc. It is also represented as $(M^{2+}_{1-\delta} M^{3+}_{\delta})$ $[M^{2+}_{\delta} M^{3+}_{2-\delta}] O^{2-}_4$, where δ represents the cation distribution between the tetrahedral A and octahedral B sites. The simple bracket represents the average occupancy of A sites and the square bracket represents the average occupancy of B sites. The inversion parameter is $\delta = 0$ for normal spinels, 1 for inverse spinels, and between 0 and 1 for mixed spinel structures. Selective incorporation of metal ions in the tetrahedral and octahedral sites of the spinel structure allows the creation of many different materials having properties that can be tailored to a variety of applications.

$Ni_x Zn_{1-x} Fe_2 O_4$ (x = 0.65) is an example of mixed spinel structured material that comes under the class of soft ferrites. Nickel zinc ferrite (NZFO) is a material of high saturation magnetization, low eddy current loss,

*Correspondence: jgadoor@gmail.com

low coercivity, high Curie temperature, high resistivity, low dielectric loss, low dielectric constant, good thermal stability, and low cost. As a result, NZFO find many commercial applications such as being a noise suppressor material in various electromagnetic interferences [1,2], cores of RF transformers and inductors, reflectance coils, antennas, and modulators [3]. NZFO also finds application in pulsed magnetic devices of accelerators and electronic switching systems [4], magnetic storage devices, microwave devices, etc. One important feature of nickel zinc ferrite is that its electrical and magnetic properties strongly depend on the distribution of cations in the tetrahedral (A) and octahedral (B) sites of the spinel structure [5–8]. There are several novel approaches of synthesis to induce tailor-made properties to nickel zinc ferrite. Controlled grain growth by the introduction of an amorphous medium is one such method. The present work is based on a procedure of synthesis in this direction, as previously reported [9–15], where a heterogeneous complex combination of polynuclear cations of Fe^{3+}, Ni^{2+}, and Zn^{2+} and glyoxylate dianion $(C_2H_2O_4^{2-})$ is used as the precursor of ferrite particles. The metal ion–glyoxylate dianion complex is uniformly disbursed in the gel medium of SiO_2. Several researchers used SiO_2 as an excellent host medium for the uniform distribution of ferrite precursor [16–20]. There are reports on the use of SiO_2 as an additive for modifying the properties of nickel zinc ferrites [21–25]. The three-dimensional network of silica medium has plenty of voids that can act as the perfect nucleation sites for the nickel zinc ferrite particles during thermal decomposition of the trapped precursor units. The silica matrix is used not only to serve as the spatial nucleation site, but also to confine the coarsening of nanoparticles and minimize the degree of crystalline aggregation. It is well known that magnetic nanoparticles tend to agglomerate not only due to their large surface energy but also due to their strong magnetic interaction. The magnetic/electric/optical properties of the medium enhances with reduction in particle size. Thus, it is necessary to keep the particle size stable against changes in different physical conditions for reproducible and identical physical properties. In this context the amorphous and nonmagnetic silica medium plays an effective role to control the particle agglomeration due to aging or changes in temperature. There are reports on the synthesis of granular ferrite particles by coating SiO_2 [26] on NZFO nanoparticles, where it is difficult to coat all particles with uniform thickness or isolate each particle and encapsulate them uniformly.

There are several studies on the effect of the silica matrix on the structural and magnetic properties of NZFO [10,11,13–15], ZFO [16,17], and NFO [18,19] by changing the ferrite content in SiO_2. It is found that the amorphous medium has a strong influence on the size of ferrite crystallites and their magnetic properties. For samples with low ferrite content, particle size is well below the critical size for observing superparamagnetism [10,11], whereas high ferrite content results in higher values of saturation magnetization and retentivity. These papers thoroughly investigated the magnetic properties of the material for different proportions of Ni, Zn, and Fe in NZFO and for different ratios of ferrite in SiO_2.

So far, no systematic study on the effect of SiO_2 medium on electrical properties of NZFO nanoparticles following the same synthesis has been reported. It is worth noting that dielectric constant, loss tangent, and conductivity are some of the characteristic properties that make a material potentially significant for different applications. NZFO is a material of low dielectric constant, very low loss tangent, and very high resistivity. The magnitude of all these quantities depends on factors such as method of synthesis, composition, Fe^{2+}/Fe^{3+} ratio, cation distribution in the octahedral and tetrahedral sites of the spinel structure, sintering temperature, particle size, and frequency of the electric field. Here we report the influence of the silica matrix on the electrical properties of ferrite by changing the ferrite content.

2. Materials and methods

The materials used in the synthesis are $Fe(NO_3)_3.9H_2O$, $Ni(NO_3)_2.6H_2O$, $Zn(NO_3)_2.6H_2O$, and tetraethyl orthosilicate (TEOS; 98% ACS reagent), all from Sigma Aldrich; ethylene glycol (GR) (99%) from Merck; and ethanol (98%). Stoichiometric estimation of reactants is based on the chemical equation reported [10–12]. The amount of TEOS used in this study corresponds to the quantity of SiO_2 in the final product. Estimated molar masses of ferric nitrate, nickel nitrate, and zinc nitrate are weighed and they are dissolved in ethanol. Ethylene glycol (molar ratio $EG : NO_3^- = 2 : 1$) is gently added under constant stirring to the above to get a clear solution. A calculated volume of TEOS in ethanol is slowly added to the ethanol-metallic nitrate-ethylene glycol mixture and stirred well for homogeneous mixing of the different constituents. The mixture is kept at 65 °C in a hot air oven for gel formation and thereafter at the same temperature for drying. The dried gel is further heated to 130 °C for the formation of a heterogeneous complex combination of polynuclear cations of Fe^{3+}, Ni^{2+}, and Zn^{2+} with glyoxylate dianion $(C_2H_2O_4^{2-})$. The SiO_2 matrix is formed by hydrolysis of TEOS from silanol monomers and then it condenses and is cross-linked to form the silica gel network [27]. The rate of gelation depends on the concentration of the reactant, the type and amount of catalyst, and the ambient temperature. According to previous reports [12], the presence of ethylene glycol in the medium influences the gelling process and the morphology of the final silica matrix. The metal nitrate-ethylene glycol complex, disbursed uniformly in the medium, gets trapped in the pores of the silica gel matrix and acts as the precursor for NZFO. Thermal decomposition of the metal-ethylene glycol complex at 350 °C results in the formation of $(Ni_{0.65}Zn_{0.35}Fe_2O_4)_x$ / $(SiO_2)_{1-x}$. The sample is further sintered at temperatures of 600, 800, 900, 1000, and 1100 °C for 3 h for better crystalline phase formation. The synthesized final products with different $(ferrite)_x$ / $(SiO_2)_{1-x}$ ratios are labeled as $S_0(x = 0), S_1(x = 0.15), S_2(x = 0.35), S_3(x = 0.50), S_4(x = 0.65), S_5(x = 0.85)$, and $S_6(x = 1)$.

3. Characterization

Thermal decomposition of the reactants, elimination of volatile byproducts, and the evolution of stable end products are investigated using thermogravimetric and derivative thermogram analysis. Fourier transform infrared studies are performed to monitor the functional groups present during different stages of development of NZFO samples. For the structural studies, powder XRD is used as the primary technique and TEM imaging is used as a complementary tool. Morphological studies are done using transmission electron diffraction analysis. Electrical studies are conducted using a Hioki 3532-50 LCR Hi-Tester LCR meter. For the electrical study, $Ni_xZn_{1-x}Fe_2O_4$ / SiO_2 powder is mixed with PVA binder and compacted to a disc shape of thickness of 2 mm and diameter of 13 mm by applying pressure of 5 t for 5 min. The pellet is annealed at 850 °C for 3 h for the removal of the binder. XRD values of the crushed pellet are taken to study the effect of high pressure and temperature on the material. No modification is observed in the diffraction pattern, inferring the stability of the material against compressing at 5 t or annealing at 850 °C. Silver paste is applied on the top and bottom sides of the pellet and it is loaded into the sample holder for electrical measurements. The sample and the holder are then transferred to a temperature-controlled heater unit attached to the LCR meter for electrical property studies.

4. Results and discussion

4.1. Thermal analysis

Thermogravimetric analysis is carried out using the PerkinElmer model STA 6000 instrument. A dried gel sample of known mass is heated in a cylindrical platinum crucible to 750 °C at the rate of 10 °C /min in

a nitrogen environment. Two samples of nickel zinc ferrite, S_2 and S_6, are chosen for the study. Analysis of TG/DTG curves can be summarized as follows. For sample S_2 (as shown in Figure 1), three peaks are observed at 138.69 °C, 167.12 °C, and 376.37 °C in DTG, while TG shows continuous loss of mass up to 550 °C and a nearly stable state thereafter.
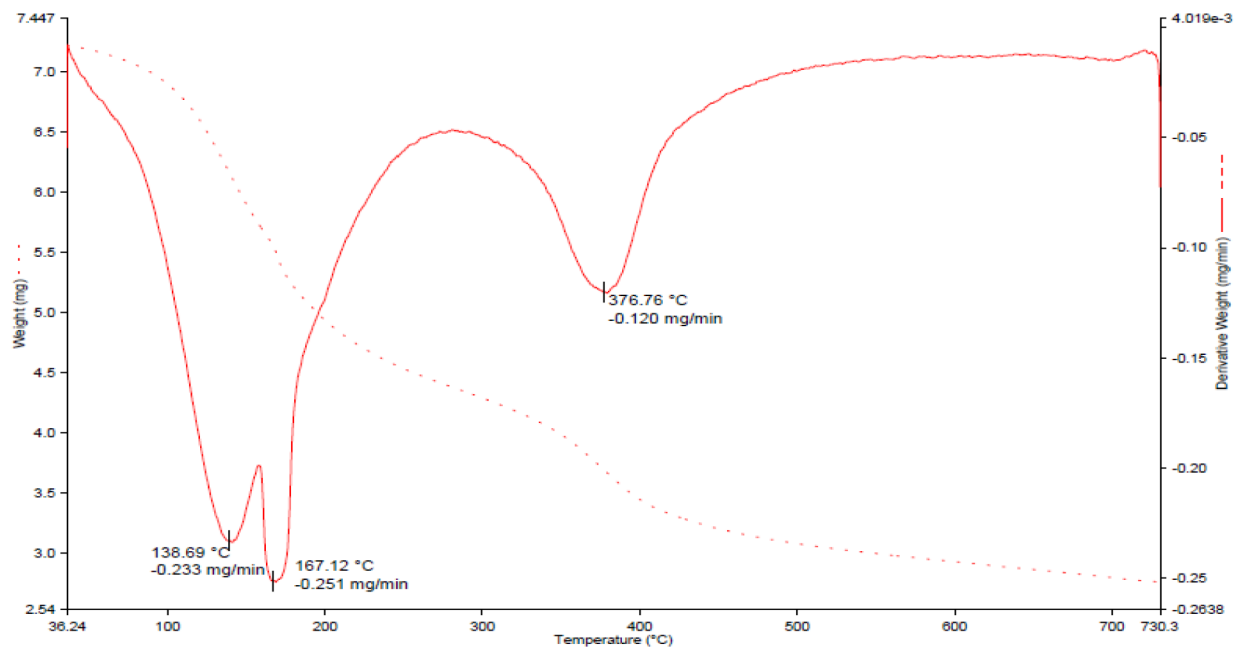

Figure 1. TGA/DTG of sample S_2.

1. It is expected to form a metal-ethylene glycol complex along with NO, HNO_3, water, and ethanol in the initial state of synthesis [10,12], so the reaction peak at 138.69 °C with mass loss of 0.233 mg/min is due to the oxidation reaction of metal nitrates with the elimination of volatile components of the reaction product [10,12,28–30].

2. Derivative mass loss of 0.25 mg/min at 167.12 °C and the loss of weight in the TG graph up to 200 °C are assigned to elimination of HNO_3, the unreactive part of TEOS, and other volatile components of reaction products.

3. Loss of weight of 0.12 mg/min at 376.37 °C is due to the oxidative decomposition of the metal-ethylene glycol complex, leading to the formation of the ferrite phase and elimination of volatile components CO and H_2O [28,29].

Sample S_6 (shown in Figure 2) has two prominent loss peaks at 145.7 °C and 359.49 °C along with two minor peaks at 194.780 °C and 503.490 °C in DTG, while the TG curve shows continuous weight loss up to 550 °C and a nearly stable state after that.

1. Formation of the metal-ethylene glycol complex along with the removal of volatile components NO, ethanol, and water results in the loss of weight of 0.113 mg/min at 145.7 °C.

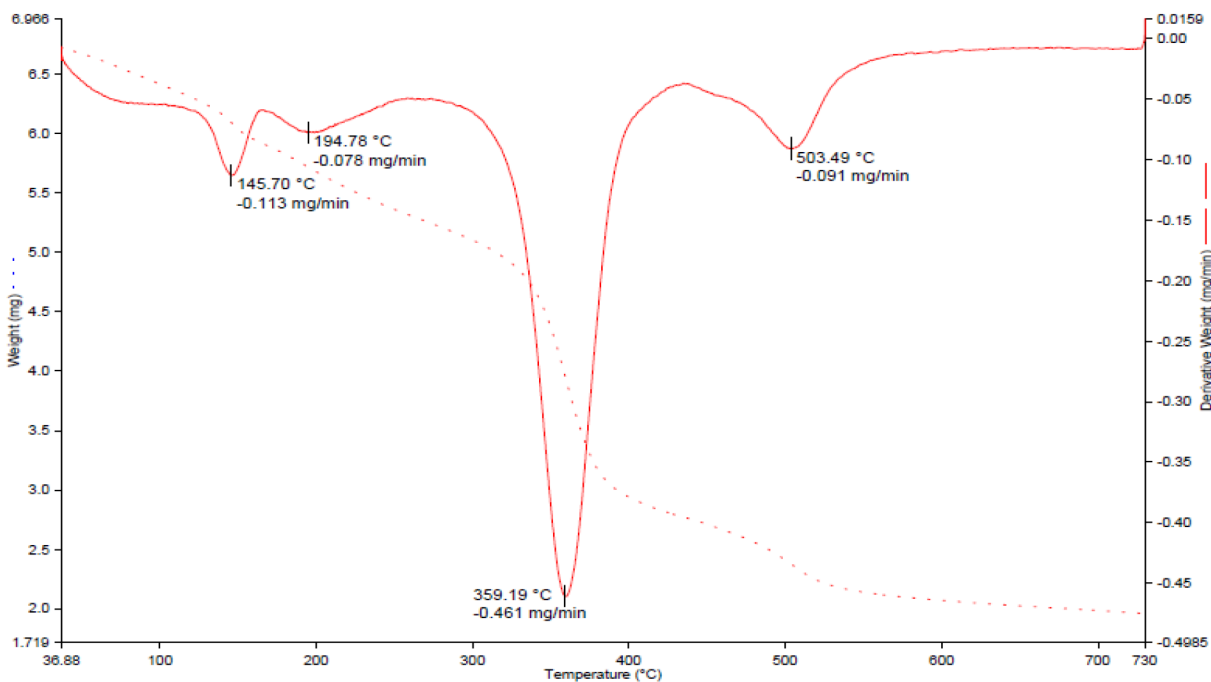2. Loss of weight of 0.078 mg/min at 194.78 °C is assigned to the elimination of excess ethylene glycol and HNO_3.

Figure 2. TGA/DTG of Sample S_6.

3. The third peak at 359.19 °C with a loss of 0.461 mg/min shows thermal decomposition of the metal-ethylene glycol complex to the ferrite phase and elimination of volatile components CO and H_2O.

4. The observed weight loss of 0.091 mg/min at 503.49 °C is due to thermal decomposition of excess nickel nitrate, if any, to nickel oxide after the formation of ferrite [31].

4.2. FT-IR analysis

Fourier transform infrared absorption analysis provides information about the functional groups present during the different stages of the development of a sample. The spectrum is recorded by a Thermoavatar 370 spectrophotometer, using KBr pellets in the range of 400–4000 cm^{-1}. Three samples of S_2 selected during different stages of synthesis of NZFO and that of sample S_0 are used for the analysis. Characteristic spectra of S_2 (x = 0.35) at three stages of thermal processing are shown in Figures 3–5 and Table 1 shows their corresponding absorption bands. The absorption frequencies in the last column of Table 1 are of sample S_0 (Figure 6), for identifying the functional groups due to the host medium. The broad and intense absorption bands at 3400 cm^{-1} and 1640 cm^{-1} are due to $H-O-H$ stretching and bending vibrations. The band at 1380 cm^{-1} due to symmetric stretching of the $N-O$ bond in NO_3^- is clearly present in Figure 3. It is weak in Figure 4 and absent in Figure 5, indicating the consumption of NO_3^- during oxidation of ethylene glycol at higher temperatures [10,12,14]. The broad high-intensity peak at 1080 cm^{-1} with the accompanying shoulder at 1200 cm^{-1} is due to the asymmetric LO and TO stretching bond of $\equiv Si-O-Si \equiv$ of the SiO_4 tetrahedron associated with the motion of oxygen in $Si-O-Si$ asymmetric stretching [20,27,32–35]. Characteristic absorption bands of symmetric $Si-O-Si$ stretching, $Si-O-Si$ bending, and $Si-O-C_2H_5$ and OH^- stretching vibrations at 786 cm^{-1}, 461 cm^{-1}, and 442 and 1638 cm^{-1} are in agreement with the above reference. The functional group
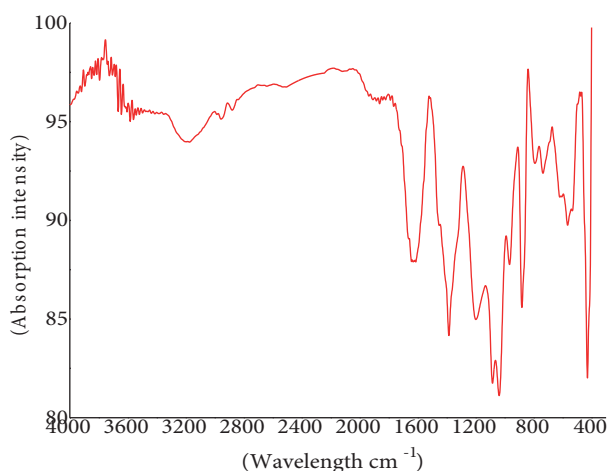
Figure 3. Sample S_2 at 65 °C.
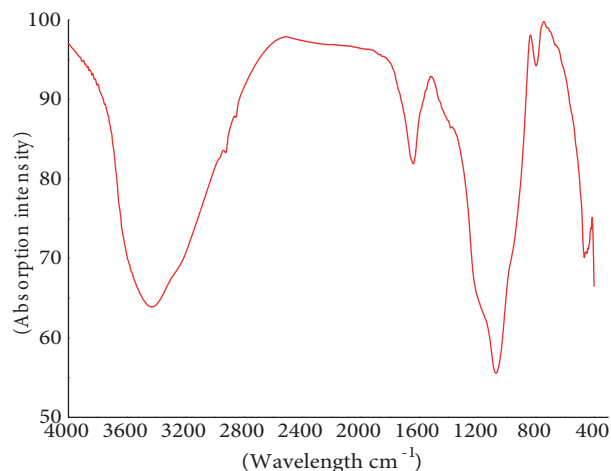
Figure 4. Sample S_2 at 275 °C.
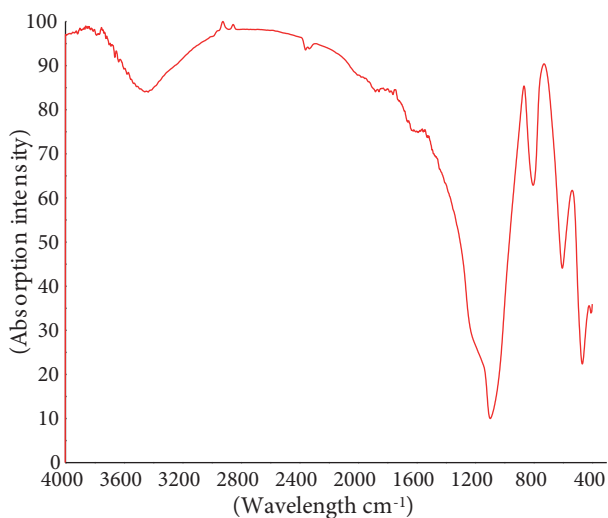
Figure 5. Sample S_2 at 1000 °C.
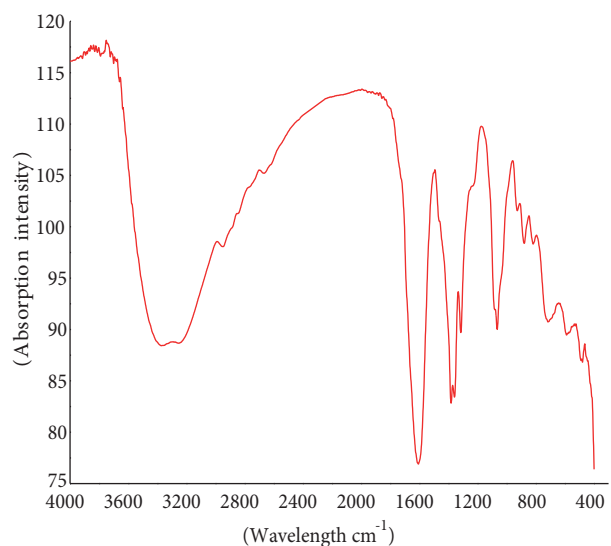
Figure 6. Sample S_0 at 65 °C.

COO^- in the metal-glycol complex has a characteristic asymmetric vibration at ~ 1620 cm^{-1} and the OH^- stretching vibration in H_2O has absorption at ~ 1640 cm^{-1}. Intensities of these vibrations are sufficiently strong in Figure 3 due to their overlapping effect [14]. At higher processing temperatures these vibrations are no longer present, confirming the thermal decomposition of the metal-glycol composite. Absence of absorption band ν(C-O) of the glycol group at ~ 1028 cm^{-1}, stretching vibrations of H_2O at ~ 1640 cm^{-1}, and Si – O – C_2H_5 at 2978 cm^{-1} and 2896 cm^{-1} at higher processing temperatures reveal the thermal decomposition of the metal-glycol complex and condensation of TEOS to silica matrix. Absorption bands at ~ 1080 cm^{-1} and 590 cm^{-1} correspond to the fingerprint of Si – O – Si vibration. The sample processed at 1000 °C (Figure 5) shows only a few intense absorption bands, confirming the signature frequencies of the metal-oxide phase, Si – O – Si, and low intensity of –OH and –COH vibrations bands infers the presence of the ferrite phase in the silica matrix. The observed absorptions at 560 and 467 cm^{-1} are assigned to characteristic vibrations of metal ions in the tetrahedral or octahedral sites of the spinel structure [14,32]. γFe_3O_4 and Fe_3O_4 are two possible

phases in the sample, but their characteristic frequencies at 720 cm^{-1} and 570 cm^{-1} [36,37] are absent in sample S$_2$ annealed at 1000 °C, confirming the phase purity of the final product. The analysis clearly confirms the presence of the ferrite phase and the silicon dioxide matrix.

Table 1. Prominent absorption bands of samples S$_2$ and S$_0$.

Sr. no.	S$_2$ 65 °C	S$_2$ 275 °C	S$_2$ 1000 °C	S$_0$ 65 °C	Assignments, cm^{-1}
1	3174	3430	3435	3388	3400 ν (–OH)
2	2957	2923	-	2950	2935 ν_{as} (–CH)
3	2877	2863	-	2883	2870ν_s (–CH)
4	-	1640	-	1648	1640 δ (H − O − H)
5	1613	-	-		1620 ν_{as} (–COO)
6	-	-	-	1458	1462 δ (CH$_2$)
7	-	-	-	1400	1410 δ (COH)
8	1385	1382	-		1380 ν (NO$_3^-$)
9				1208	1200 ρ (CH$_2$)
10	-	1071	1097	1085	1080 ν_{as} (Si − O − Si)
11	1028	-	-	1043	1040 ν (CO)
12	881	-	-	882	882 ρ (CH$_3$)
13	788	795	804		786 ν_s (Si − O − Si) + ν (–MO)
14	736	-	-		720 (γ Fe$_2$O3)
15	-	-	604		600 ν_1 (–MO)
16	567	-	-	590	570 ν_1 (Fe$_3$O$_4$)
17	-	467	468		450 ν_2 (–MO)
18	428	-	-	450	442 ν_{as} (Si − O − C)

4.3. XRD analysis

The X-ray diffraction studies are carried out using Cu-K$_\alpha$ radiation of wavelength λ = 1.5406 nm with a Bruker AXS D8 Advance instrument for a scan angle range of 10° to 70°. Samples calcined at 400 °C and further sintered at 500, 600, 700, 800, 900, 1000, and 1100 °C are used for the study. The X-ray diffraction patterns of ferrite/SiO$_2$ samples with different ferrite contents are shown in Figure 7. From the patterns it is clear that the height (intensity) and width (FWHM) of the peak depends on the value (x) of ferrite content in ferrite/SiO$_2$. The smaller the value of x, the more spatially separated are the ferrite crystallites, so the peaks are of low intensity and broad. The intensity of a diffraction pattern at a particular Bragg angle depends on the number of scattering centers in the medium. All the reported works regarding X-ray analysis of ferrite/silica composites treated the SiO$_2$ matrix as amorphous [9–20]. Hence, the intensity of the X-ray at any Bragg angle is contributed by both the ferrite phase and the background amorphous medium. If the crystallite size is too small, then diffraction intensity becomes well below the detection limit of the instrument, resulting in a diffused pattern. Thus, the broad diffraction peaks with low intensity clearly indicate the small size of crystallites or the amorphous nature of the sample. Figure 7 shows that all diffraction peaks are matching well in terms of Bragg angle and are labeled properly using Miller indices. It is also observed that the intensity of all diffraction peaks is enhanced uniformly and the full width at half maximum of the peak reduces with the increase of ferrite content in ferrite/SiO$_2$ samples. The result agrees with the JCPDS 008-0234 data card of nickel-zinc-ferrite. The influence of thermal processing on the ferrite/silica sample is revealed in Figure 8, where XRD of samples at different sintering temperatures is shown. It is apparent that the crystallinity of the material improves further

with increase in sintering temperature. All patterns are properly labeled in terms of the (hkl) plane index. As sintering temperature increases, the height of the diffraction peak increases and the FWHM decreases but the diffraction angle maintains the same. The lattice parameter of the composite is calculated using the formula $a = \frac{\lambda\sqrt{h^2+k^2+l^2}}{2\sin\theta}$, where λ is the wavelength of the X-ray, (h, k, l) are the Miller indices of the crystal plane, and is θ the Bragg angle. For sample S_2 (sintered at 1000 $^\circ$C), the lattice parameter is 8.391 Å and it differs by 0.01 Å from previously reported results [28–30]. In these references the ferrite precursor is the same and a silica medium is absent, so the close agreement of the lattice parameter indicates that the crystalline structure of ferrite is not affected by the silica medium. Absence of impurity peaks of $NiFe_2O_4$, $ZnFe_2O_4$, Fe_2SiO_4, Ni_2O_3H, or γFe_2O_3 in the diffraction pattern of sample S_2 sintered at 1000 $^\circ$C shows the phase purity of the material, supporting the two-step thermal processing followed here [13,14]. The possibility of a characteristic diffraction pattern of βSiO_2 reported previously [10] is not observed in this case because of the lower sintering temperature employed. Samples sintered at lower temperatures show low-intensity diffraction peaks of large full width at half maximum, indicating incomplete crystallinity or small crystallite size. The average size (D) of the crystallite is calculated according to the Scherrer formula, $\beta_{hkl} = \frac{0.94\lambda}{D\cos\theta}$, where β_{hkl} is the full width at half maximum of the intense peaks, λ is the wavelength of the X-ray, and θ is the Bragg angle for the prominent peaks representing (220), (311), (400), (422), (511), and (440) planes. Table 2 shows the size of the crystallite at different sintering temperatures of sample material S_2 and the observed values are much lower than those of other methods of synthesis [9,15,38]. The observed line broadening of diffraction peaks is the resultant effect of the measuring instrument and lattice imperfection/defects of the material. Sample-dependent line broadening is due to strain induced by the crystal imperfection and the true size of the crystallite. Considering the crystallite as an isotropic medium, the strain associated is given by $\epsilon = \frac{\beta}{4\tan\theta}$. Assuming that the crystallite size and strain contribution to the line broadening are independent of each other, the observed line broadening is calculated by $\beta_{hkl measured} = \frac{4\lambda}{D\cos\theta} + 4\epsilon\tan\theta$, which is called the Williamson–Hall (W-H) equation [39,40]. From the slope and Y-intercept of the linear plot, one can find the crystallite size and lattice strain. Table 2 shows the crystallite size determined using the Scherrer equation and W-H equation and the observed lattice strain. Furthermore, the crystallite size and strain modification with sintering temperature are tabulated (Table 3). The usefulness of the W-H method depends on the number of well-developed diffraction peaks and the accuracy of FWHM measurement. At low sintering temperatures or at low ferrite contents in the sample only two or three peaks are well resolved, so the number of data points in the W-H plot are only that much and hence the accuracy of the best-fit linear plot is not very good. It is observed that crystallite size increases with increase in sintering temperature or ferrite content in the ferrite/SiO_2 sample, which agrees with reported results [9–15]. The value of crystallite size observed is in the range of 5–26 nm for samples S_1 to S_6 sintered at 1000 $^\circ$C and 5–16 nm for sample S_2 at sintering temperatures of 800–1100 $^\circ$C. Both the Scherrer equation and the W-H method give nearly the same value of crystallite size and the difference between the two results is high when the sintering temperature or the ferrite content in the composite is low. Observed strain on the crystallite is at minimum in the case of the sample without silica medium and maximum for sample S_4, where the ferrite content is 65% of the composite. It is also observed that strain on the crystallite decreases with decrease of ferrite content in the NZFO/SiO_2 medium. The spatial separation of ferrite crystallite in the composite medium and its size are the factors that decide the strain. In the case of a low ferrite/SiO_2 ratio, the crystallite is small enough to reside well in the voids of the SiO_2 matrix. As the content of ferrite in the ferrite/SiO_2 sample increases, number density and crystallite size of ferrite units increase, so the voids in the SiO_2 network are more tightly filled and

strain on the crystallite increases. The shrinkage of the SiO_2 network during thermal treatment may act on the ferrite structure and introduce strain on the lattice. It may also be possible that the SiO_2 network surrounding the crystallite is disrupted by the sintering process and crystallite size increases due to coalescence of ferrite grains and strain on the crystallite due to the medium increases.

Table 2. Crystallite size of NZFO sample S_2 at different sintering temperatures.

| Sample label | Sintering temperature (°C) | Crystallite size (nm) | | Strain ε |
		Scherrer	W-H	
S$_2$	1100	14.97	16. 7	0.029
	1000	10.68	10.3	0.015
	900	7.45	8.57	0.005
	800	5.25	2.8	0.178

Table 3. Crystallite size of NZFO in the ferrite/SiO_2 samples sintered at 1000 °C.

| Sample | Particle size (nm) | | Strain (ε) |
	Scherrer	W-H	
S$_1$	4.90	-	0.015
S$_2$	10.68	10.3	0.015
S$_3$	12.36	12.68	0.0125
S$_4$	11.13	12.39	0.079
S$_5$	17.03	18.33	0.025
S$_6$	26.43	26.49	0.0125

4.4. TEM analysis

TEM images are recorded with a JEOL JEM-2100 microscope using 200 kV electron beams for the highest resolution of nanosized particles. Information from TEM analysis is used to complement the results of X-ray powder diffraction patterns. TEM images of sample (Ni-Zn-Ferrite)$_x$ / (SiO2)$_{1-x}$ with x = 0.35 and sintered at 1000 °C are presented in Figures 9 and 10. The HR-TEM very clearly shows the distribution of ultrafine spherical particles of almost uniform size dispersed throughout the silica matrix medium. Using four TEM images, the average particle size from 60 measurements of sample S_2 sintered at 1100 °C is 18.16 ± 5.41 nm; the value so obtained is slightly higher than the results from the Scherrer and W-H equations. The average particle size of 60 measurements from four TEM images for sample S_5 sintered at 1100 °C is 21.01 ± 6.87 nm, again inferring an increased size of particles for high Ferrite/SiO_2 ratios. Thus, the effect of the silica medium is to minimize the size of the ferrite particles in the synthesized material and this is in agreement with previous reports [11,14]. The selected area diffraction (SAED) pattern in Figure 11 shows spotty concentric rings, revealing their crystalline quality. The diameter of each spotty concentric ring is measured. Using the ratio of these measurements, the corresponding crystal planes are identified as (220), (311), (400), (440), and (511).

4.5. Electric conductivity

Conductivity (σ) in general is a complex quantity and is represented as $\sigma = \sigma_{(dc)} + j\sigma_{(ac)}$. The real part of conductivity has two components, $\sigma_{(dc)} = \sigma_{(dc)} + \sigma_{(ac)}$. The dc conductivity ($\sigma_{dc}$) depends on drift mobility
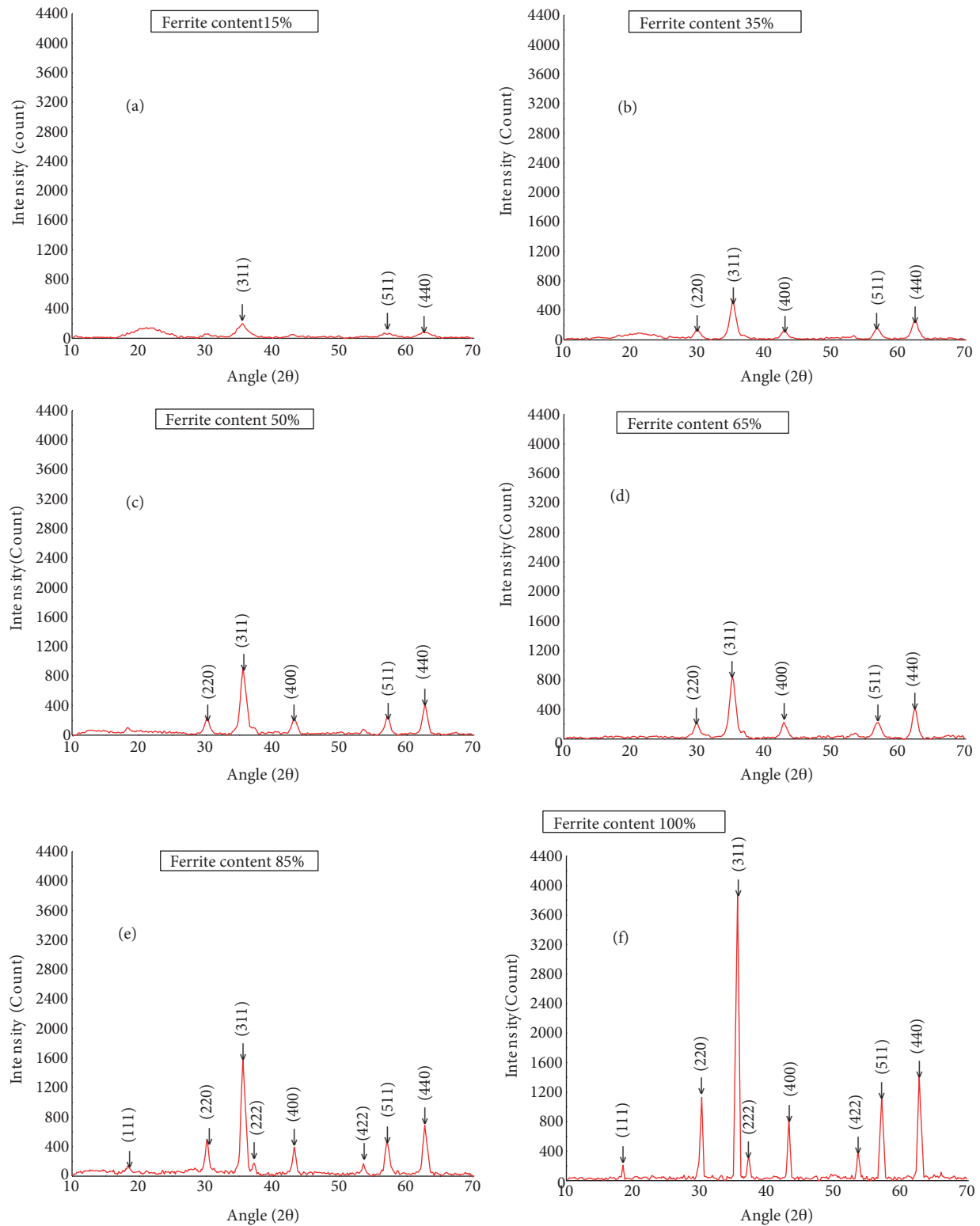
Figure 7. XRD of $(Ni_{0.65}Zn_{0.35}Fe_2O_4)_X/(SiO_2)_{1-x}$ sample sintered at 1000 $^\circ$C with different ferrite contents (a–f).
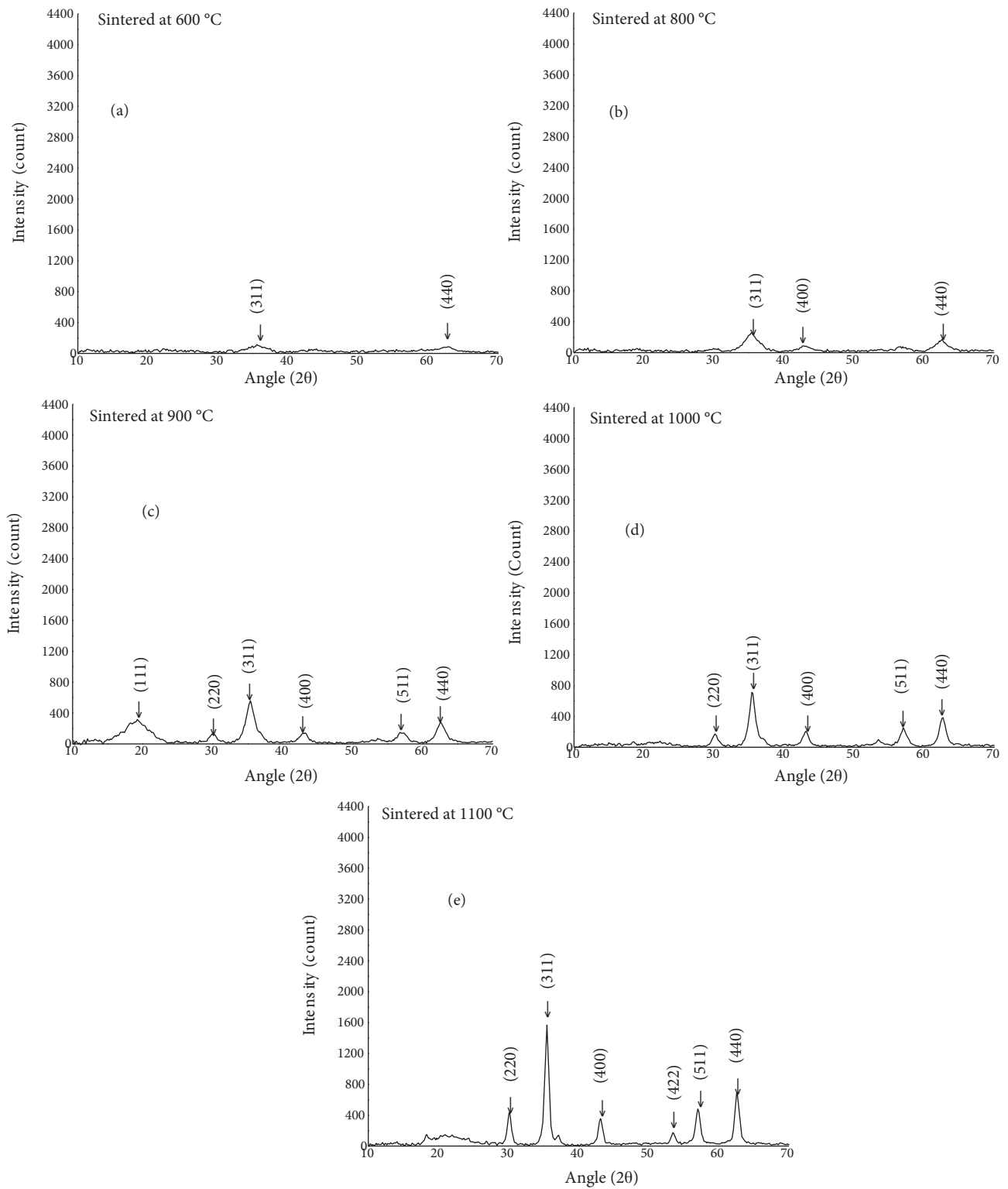
Figure 8. XRD of $(Ni_{0.65} Zn_{0.35} Fe_2 O_4)_{0.35} /(SiO_2)_{0.65}$ at different sintering temperatures (a–e).
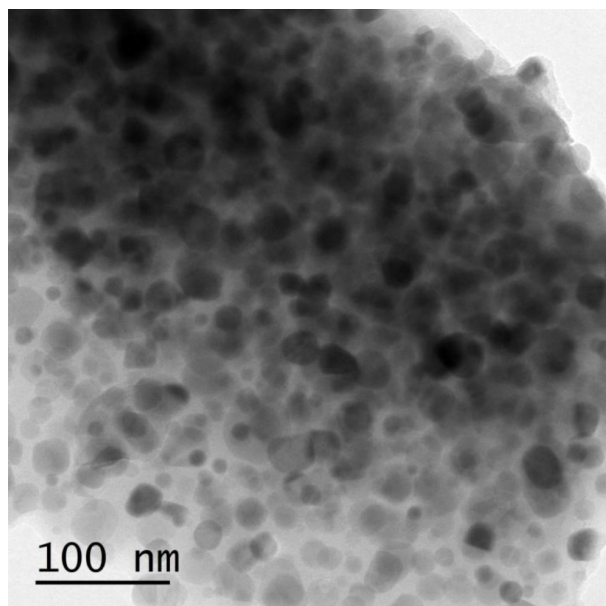
Figure 9. HR-TEM image of
$(\mathrm{Ni}_{0.65}\,\mathrm{Zn}_{0.35})_{0.35}\,/(\mathrm{SiO}_2)_{0.65}$, magnification 100 nm.
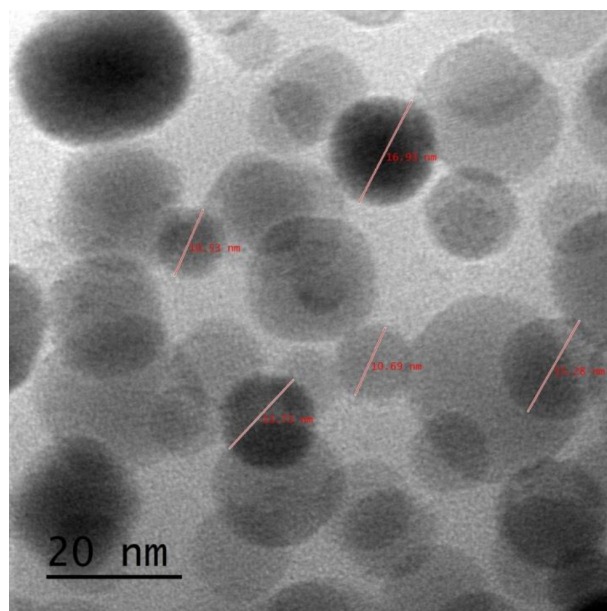
Figure 10. HR-TEM image of
$(\mathrm{Ni}_{0.65}\,\mathrm{Zn}_{0.35})_{0.35}\,/(\mathrm{SiO}_2)_{0.65}$, magnification 20 nm
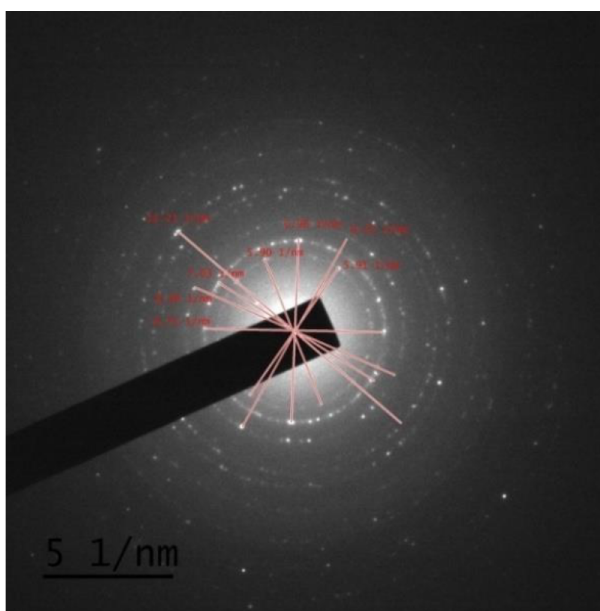

Figure 11. SAED pattern of $(\mathrm{Ni}_{0.65}\,\mathrm{Zn}_{0.35})_{0.35}\,/(\mathrm{SiO}_2)_{0.65}$.

of charge carriers and is a function of temperature, whereas the ac conductivity depends on both temperature and frequency. The ac conductivity can be determined from the dielectric constant and frequency using the relation $\sigma_{ac} = \omega\varepsilon'' = \omega\varepsilon'\tan\delta$, where $\varepsilon', \varepsilon'', \omega$, and $\tan\delta$ are the real and imaginary parts of the dielectric constant, angular frequency of the electric field, and the loss tangent, respectively. Further, σ_{ac} is attributed to the dielectric relaxation caused by the localized charge carriers and obeys a power law of the form $\sigma_{ac} = A\omega^s$, where A is a constant for a particular temperature and s represents the degree of interaction between the mobile ions and the environment surrounding them [41,42].

The atomic level occupancy of ions in NZFO crystal can be described by the structural formula $(Me_{1-\delta}^{2+} Fe_\delta^{3+})^A$ $[Me_\delta^{2+} Fe_{2-\delta}^{3+}]^B$ O_4^{2-} [43,44], where A and B stand for tetrahedral and octahedral sites, where δ is the inversion parameter and Me the divalent cations. In NZFO crystallites the Zn^{2+} cations prefer to occupy the tetrahedral and Ni^{2+} the octahedral sites, whereas Fe^{3+} is equally distributed in both sites [44–47]. In the present study the inversion parameter is 0.65; because of the strict preferential site occupancy of zinc ions and the stoichiometric relation, it is expected that 0.35 mol of Zn^{2+} ions are present in the tetrahedral A sites for every 0.65 mol of Ni^{2+} and 2 mol of Fe^{3+} ions in the NZF/SiO_2 composite. Based on activation energy and drift mobility calculation [48], it reported that the conduction mechanism in ferrite is due to hopping of charge carriers and not band conduction of free electrons/holes and now it is the generally followed explanation. Hopping probability of electrons/holes between the ions of the same element existing in two different valence states depends on the cationic distance, which in turn depends on the ionic radius, in the A and B sites. The ionic radius of cations of the nickel-zinc-ferrite unit are Zn^{2+} (=0.82 Å) > Ni^{2+} (=0.78 Å) > Fe^{3+} (=0.67 Å). From the configuration and geometry of tetrahedral and octahedral voids, the spatial separation between metallic ions in the A site is more than that of the B site. Thus, the hopping probability of electrons/holes between the ions of the same element in the A site is less than that of the B site. In the octahedral site there exist two possible metal-ion oxygen configurations. The configuration of Fe^{3+} – O is such that the bond length separation between Fe^{3+} ions is less than that between Ni^{2+} ions [48]. Thus, the probability of electron hopping between $Fe^{3+} \leftrightarrow Fe^{2+}$ is more than that of holes exchanging between $N^{2+} \leftrightarrow Ni^{3+}$. The existence of Fe^{2+} is attributed to loss of zinc during sintering (temperature above 1000 °C) or partial reduction of Fe^{3+} [43]. Oxidation of Ni^{2+} to Ni^{3+} is due to interaction of chemisorbed oxygen with the nickel ion in the NZFO structure [49,50]. The reported value of activation energy for electron hopping between $Fe^{3+} \leftrightarrow Fe^{2+}$ in $Ni_{0.65} Zn_{0.35} Fe_2 O_4$ is 0.64 eV for the sample sintered at 1200 °C [48]. The number of Fe^{2+} and Ni^{3+} ions in ferrite depends on the preparation conditions, sintering temperature, defects, etc.; hence, the conductivity of NZFO is controlled by all these factors. The movement of electrons/holes thus generated is restricted within the limit of the crystallites. According to Koop's theory [51], each ferrite grain has a conducting volume space with a highly resistive boundary surface. In an applied electric field the ferrite grain can be polarized and the conductivity of ferrite depends on the extent of space charge polarization of the medium. Observations regarding conductivity of the material as a function of frequency for different ferrite/SiO_2 ratios are presented in Figures 12 and 13.

Both figures show the same nature of variation in conductivity with frequency, which is the typical characteristic behavior of NZFO [41,42,52–54], whereas that for the ferrite/SiO_2 ratio is different in the two graphs. Figure 12 shows that conductivity increases with increase in ferrite content while Figure 13 shows behavior in the opposite way. From crystallite size and grain size determination it is observed that the size of the ferrite/SiO_2 composite increases from sample S_1 to S_6. The smaller the crystallite size, the lower the number cations and hence a limited amount of hopping of charge carriers. As the number of ferrite ions increases with particle size, an increased amount of electron hopping between $Fe^{3+} \leftrightarrow Fe^{2+}$ in the octahedral sites is expected and thus conductivity is enhanced, as observed in Figure 12. The size of crystallites S_5 and S_6 from XRD is 17 and 26 nm, respectively, and the average grain size of S_5 from HR-TEM is 21 ± 6.9 nm. Thus, the contact area between two grains and the number of ferrite/SiO_2 composites in contact increase with an increase in ferrite content in the composite. The advantage of enhancement in conductivity with increase in area at a single contact point is negated by the increased number of contact points between grains. Hence,
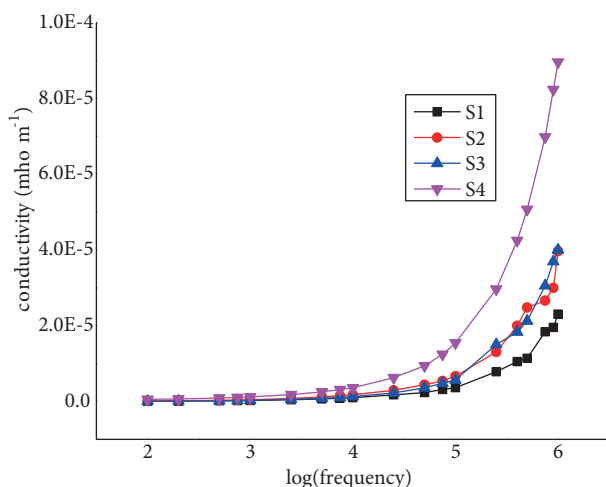
Figure 12. Conductivity of samples S_1, S_2, and S_3 at different frequencies of electric field.
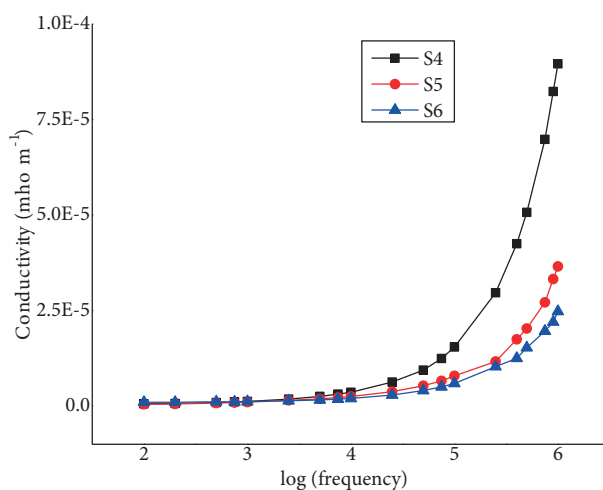

Figure 13. Conductivity of samples S_4, S_5, and S_6 at different frequencies of electric field.

conductivity decreases, as observed in Figure 13. A ferrite compact can be assumed as a series of conducting and nonconducting regions similar to that of a multilayer capacitor, the impedance of which decreases with increase in the frequency of the applied field. In other words, the high frequency field acts as a pumping force for pushing more localized charges and hence mobility and conductivity increase with the frequency of the field, which agrees with Figures 12–14. As the ferrite content in the sample increases, conductivity increases with temperature. If the thermal energy $(k_B T)$ associated with a ferrite particle at temperature T is greater than the activation energy for charge hopping, conductivity is expected to increase, in agreement with Figure 14. The increase in conductivity may also be due to increase in drift mobility of charge carriers with temperature. For low ferrite concentrations, it is the number of ferrite particles and not the temperature that decides the conductivity. Figure 15 illustrates this observation. If σ_{sx} represents the conductivity of the different ferrite/SiO$_2$ composites then it is observed that $\sigma_{s4} > \sigma_{s5} > \sigma_{s6}$ and $\sigma_{s4} > \sigma_{s3} > \sigma_{s2} > \sigma_{s1}$. The lattice strain (S$\varepsilon$) resulting from the W-H equation for different ferrite/SiO$_2$ composites can be written as $S_{\varepsilon4} > S_{\varepsilon5} > S_{\varepsilon6}$ and $S_{\varepsilon4} > S_{\varepsilon3} > S_{\varepsilon2}$ and $S_{\varepsilon1} > S_{\varepsilon2}$. The resemblance in the two inequality relations indicates that the silicon dioxide matrix has some role in the conductivity of the ferrite medium.

4.6. Dielectric constant

One of the most important properties of a material that characterize its technological value is the dielectric constant. There are many factors, such as method of preparation, additives, sintering temperature, microstructure, conductivity, and frequency, that determine the dielectric behavior of a material. Consequently, there is no unique value for the dielectric constant of NZFO. The dielectric aspect of a material is associated with the polarization of the medium, which in general has four components, interfacial, dipolar, electronic, and ionic polarization; all of them are frequency-dependent. In ferrites space-charge polarization is the dominant factor that decides the dielectric properties of the medium. The observed dielectric constant of ferrite/SiO$_2$ samples as a function of frequency is shown in Figures 16 and 17.

As expected, both graphs describe the typical inverse dependence of the dielectric constant on frequency [22,40,41,55,56]. At low frequencies contributions from all four components of polarization of ferrite are present and the value gradually falls, mainly due to the fall in the share from the space-charge component. The time
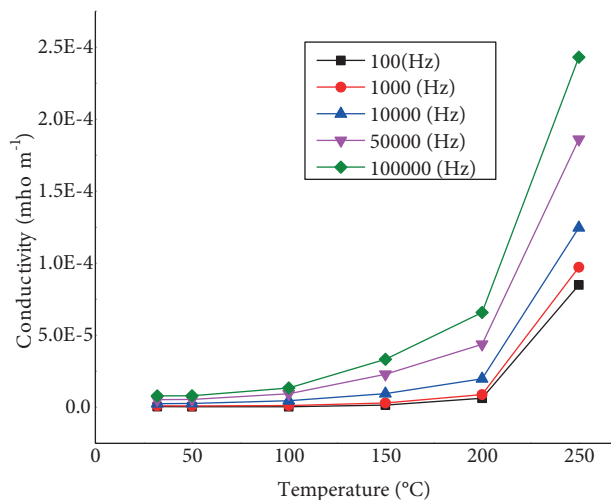
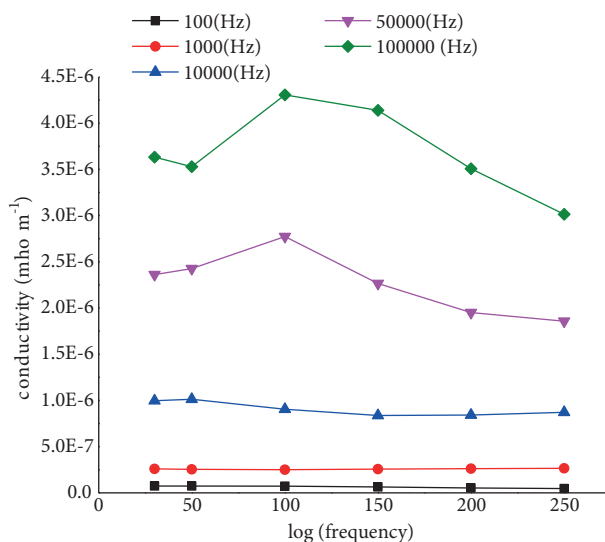**Figure 14.** Conductivity of sample S_5 at different temperatures.

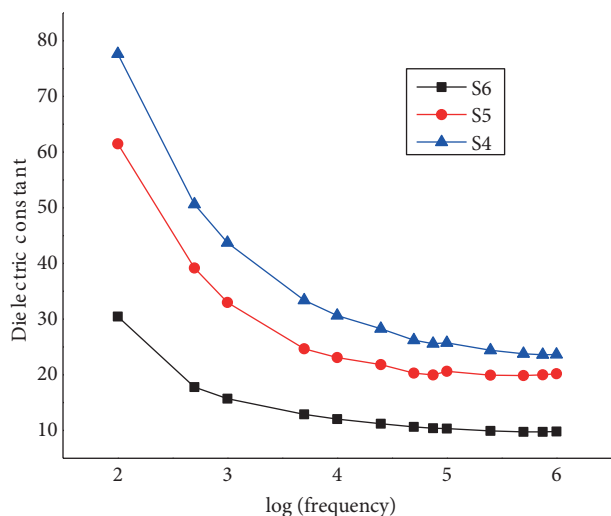**Figure 15.** Conductivity of sample S_1 at different temperatures.

Figure 16. Dielectric constant of sample S_4, S_5, and S_6 at different frequencies of electric field.
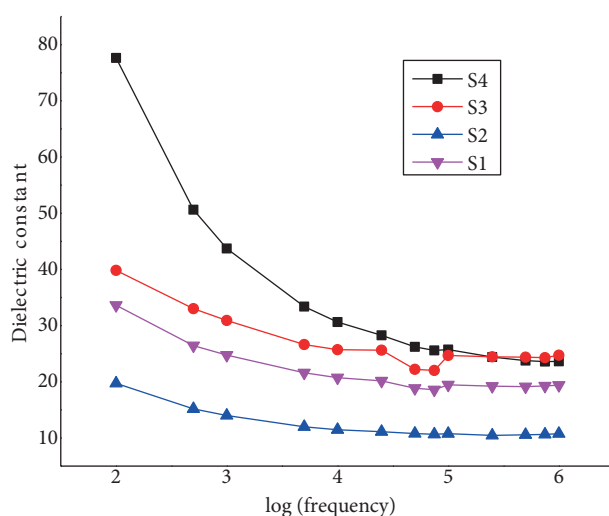

Figure 17. Dielectric constant of sample S_4, S_3, S_2, and S_1 against frequencies of electric field.

delay in responding to high-frequency alternating fields is strong for interfacial (space-charge) polarization; hence, the dielectric constant decreases with increase in frequency. At very high frequency field polarization due to ionic and electronic components can only follow the field reversal so the total polarization is much smaller than that of a low-frequency field. The nature of variation of the dielectric constant of the composite with change of the ferrite/SiO$_2$ ratio can be summarized as $\varepsilon_4 > \varepsilon_5 > \varepsilon_6$ from Figure 16 and $\varepsilon_4 > \varepsilon_3 > \varepsilon_1 > \varepsilon_2$ from Figure 17. The observed value strain (Sε) of the crystallite is $S_{\varepsilon 4} > S_{\varepsilon 5} > S_{\varepsilon 6}$ and $S_{\varepsilon 4} > S_{\varepsilon 3} > S_{\varepsilon 2}$ and $S_{\varepsilon 1} > S_{\varepsilon 2}$. This shows that the dielectric constant depends on the degree of polarization of the medium and also on the extent to which the crystallite is strained. The exact nature of modification of polarization of a ferrite grain under strain is a point to be explored. This also implies that the amorphous SiO$_2$ matrix has a definite contribution to the dielectric properties of ferrite.

Figures 16 and 17 show that the dielectric constant decreases with an increase in ferrite concentration, whereas the nature of variation is exactly opposite in Figure 17. The maximum value of the dielectric constant is observed for 65% ferrite in SiO_2 (sample S_4).

4.7. Dielectric loss

We know that the electric flux density and electric field are related by D $= \in E =\in_0 E + P$, where ϵ and ϵ_0 are the permittivity of the medium and free space and P is the polarization. In an applied alternating electric field, the dipole moment vector rotates and tries to remain aligned with the field. Due to the inherent inertia of dipoles there is a phase delay in the orientation of the dipole moment vector with respect to the applied field. The degree to which the dipole moment vector is out of phase with the incident electric field decides the characteristic energy loss (loss tangent) of the medium. It is also known that dielectric loss is given by the equation tan $(\delta) = \epsilon''/\epsilon'$, where ϵ' and ϵ'' are the real and imaginary parts of the dielectric constant. The loss factor is the primary criterion for the usefulness of a dielectric as an insulator material (low dielectric constant) or capacitor (high dielectric constant). In both cases it is desirable to have a very low dielectric loss tangent. An electric analog of a ferrite nanoparticle is the parallel combination of resistance and capacitance, which is represented in terms of the real part of dielectric permittivity ε' and conductivity σ. The phase delay between the respective currents is defined as $\tan\delta = \frac{capacitive\ current}{resistive\ current} = \frac{\sigma}{\omega\varepsilon'}$, from which it is obvious that $\tan\delta$ decreases with frequency since the conductivity of ferrite is very low. The nature of variation of the loss tangent with frequency is consistent with the explanation based on the electrical equivalent model of ferrite particles. It is also observed that dielectric loss decreases considerably due to the presence of the amorphous medium and takes the lowest value (less than 0.5) for highly dispersed ferrite samples S_1 and S_2. For samples with very low ferrite content, dielectric loss is very low and is nearly a constant irrespective of frequency variation. It is also observed that the loss tangent decreases with increase in temperature, as with frequency of field. Figure 18 illustrates this point. Temperature-dependent behavior of the loss tangent is shown in Figure 19 and is in agreement with the expected theoretical results.
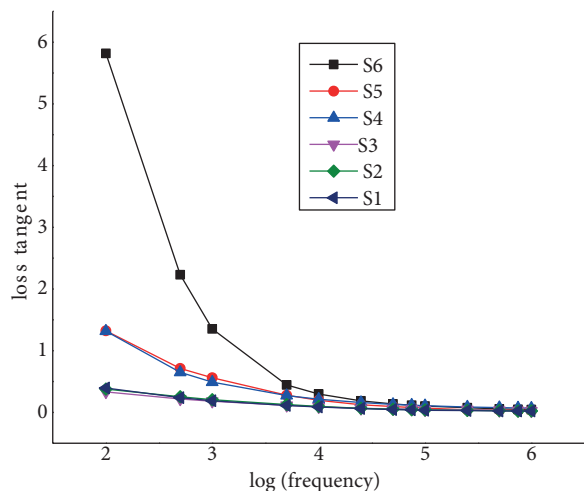

Figure 18. Loss tangent of ferrite samples at different frequencies of field.
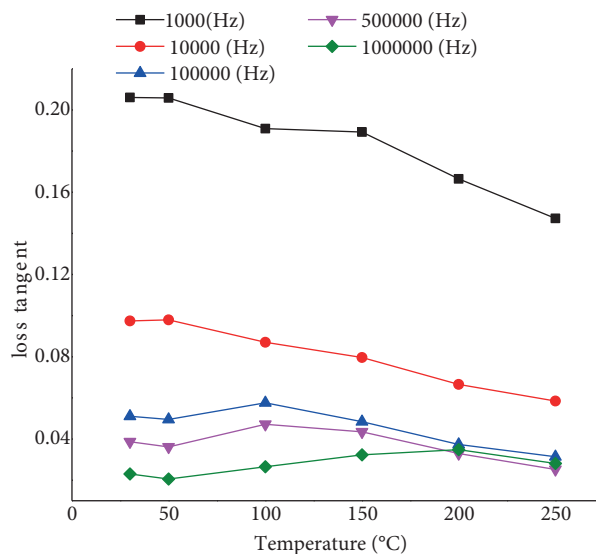
Figure 19. Loss tangent of ferrite samples S_2 at different temperatures.

5. Conclusion

$(Ni_{0.65}Zn_{0.35}Fe_2O_4)_x$: $(SiO_2)_{1-x}$ with x = 1.0, 0.85, 0.65, 0.5, 0.35, and 0.15 is synthesized using the glyoxylate precursor method for ultrafine and uniformly sized nanoparticles. TGA/DTG analysis of the sample shows stability of the product above 500 °C and FT-IR studies confirm the presence of absorption bands corresponding to characteristic functional groups of M – O vibrations and Si – O – Si vibrations. XRD and TEM analyses confirm the crystal structure as a single-phase fcc spinel NZFO, free of impurities and defects. XRD studies reveal that the crystallite size is of the nano scale in the range of 5–26 nm depending on the mass percentage of ferrite in ferrite/SiO_2 samples. The range of crystallite size is 5–16 nm for sample S_2 in the temperature range of 800–1100 °C. The average size of ferrite particles is much lower than that of other methods. Samples sintered at 800, 900, 1000, and 1100 °C with well-defined intensity peaks agree with the JCPDS standard reference. The average crystallite size of samples calculated using the Scherrer formula and W-H method is in agreement with and in the range of previous reported values [9–15]. The lattice parameter calculated for sample S_2 is 8.391 Å and it differs by 0.01 from the value reported using the same method of synthesis, except for the silicon dioxide medium. That means that the SiO_2 medium has nothing to do with the structural aspect of ferrite. Strain on the crystallite is calculated using the W-H method and it is found that the crystallite is under minimum strain in the absence of silica medium. Conductivity and dielectric constant studies reveal that they are clearly influenced by the silica medium. It is found that conductivity (10^{-5} to 10^{-4} mho m^{-1}) and the dielectric constant (30–80) are maximum for the sample with 65% ferrite (sample S_4). It is observed that the ferrite/SiO_2 composite with ferrite crystallite of maximum strain shows the highest value of conductivity and dielectric constant. The dielectric loss tangent is remarkably low with the introduction of silica medium. Thus, the role of the amorphous medium is not only to control crystallite growth at higher sintering temperatures but also to modify the electrical properties of ferrite material. Hence, this study provides an efficient and economical way of synthesis of material of low dielectric constant, very low conductivity and loss tangent, and low frequency dispersion for making good insulators.

References

[1] Yoshida, S.; Kondo, K.; Ono, H. *NEC Technical J.* **2006**, *1*, 77-81.

[2] Matsushita, N.; Kondo, K.; Yoshida, S.; Tada, M.; Yoshimura, M.; Abe, M. *J. Electroceram.* **2006**, *16*, 557-560.

[3] Murthy, V. R. K.; Viswanathan, B. *Ferrites Materials Science and Technology*; Narosa; New Delhi, India, 1990.

[4] Shinde, R. S.; Pareek, P.; Yadav, R. R. In *APAC Proceedings: 3rd Asian Conference on Particle Accelerators*; Gyeongju, Korea, 22–26 March 2004, p. 702.

[5] Su, H.; Zhang, H.; Tang, X.; Jing, Y.; Liu, Y. *J. Magn. Magn. Mater*.**2007**, *310*, 17-21.

[6] Dormann, J. L.; Nogues, M. *J. Phys. Condens. Mat. Let.* **1990**, *2*, 1223-1237.

[7] Rezlescu, N.; Rezlescu, E.; Pasnicu, M. L. *J. Phys. Condens. Mat.* **1994**, *6*, 5705-5716.

[8] Virden, A. E.; O'Grady, K. In *Proceedings of the JEMS'04 on Magnetic Symposia*; Dresden, Germany, 5–10 September 2004.

[9] Silva de Albuquerque, A.; Domingos Ardisson, J.; Bittencourt, E.; Augusto de Almeida Macedo, W. *Mat. Res.* **1999**, *2*, 235-238.

[10] Stefanescu, M.; Caizer, C.; Stoia, M.; Stefanescu, O. *J. Optoelectron. Advm.* **2005**, *7*, 607-614.

[11] Stefanescu, M.; Caizer, C.; Stoia, M.; Stefanescu, O. *Acta Mater.* **2006**, *54*, 1249-1256.

[12] Stoia, M.; Caizer, C.; Stefanescu, M.; Barvinschi, P.; Julean, I. *J. Thermal Calorim.* **2007**, *88*, 193-200.

[13] Stefanescua, M.; Stoia, M.; Caizer, C.; Stefanescu, O. *Mater. Chem. Phys.* **2009**, *113*, 342-348.

[14] Stoia, M.; Caizer, C.; Ştefănescu, M.; Barvinschi, P.; L. Barbu-Tudoran, L. *J. Sol-Gel Sci. Techn.* **2011**, *58*, 126-134.

[15] Pozo Lópeza, G.; Condó, A. M.; Urreta, S. E.; Silvetti, S. P.; Aguirre, M. C. *Mater. Charact.* **2012**, *74*, 17-27.

[16] Pascuta, P.; Vladescu, A.; Borodi, G.; Culea, E.; Tetean, R. *Ceram. Int.* **2011**, *37*, 3343-3349.

[17] Blanco-Gutierrez, V.; Torralvo-Fernandez, M. J.; Saez-Puche, R. *J. Phys. Chem. C* **2010**, *114*, 1789-1795.

[18] Carta, D.; Loche, D.; Mountjoy, G.; Navarra, G.; Corrias, A. *J. Phys. Chem. C* **2008**, *112*, 15623-15630.

[19] Perez, E.; Gomez-Polo, C.; Larumbe, S.; Perez-Landazabal, J. I.; Sagredo, V. *Revista Mexicana de Fisica S* **2012**, *58*, 104-107.

[20] Li, L.; Li, G.; Smith, R. L. Jr.; Inomata, H. *Chem. Mater.* **2000**, *12*, 3705-3714.

[21] Kotnala, R. K.; Verma, V.; Pandey, V.; Awana, V. P. S.; Aloysius, R. P.; Kothari, P. C. *Solid State Commun.* **2007**, *143*, 527-531.

[22] El Kony, D.; Saafan, S. A. *J. Am. Sci.* **2012**, *8*, 10.

[23] Uzma, G. *Indian J. Pure Ap. Phy.* **2015**, *53*, 271-273.

[24] Saadon, A. K. *Ibn al-Haitham Journal for Pure and Applied Sciences* **2012**, *3*, 25.

[25] Hajalilou, A.; Hashim, M.; Ebrahimi-Kahrizsangi, R.; Sarami, N. *J. Phys. D Appl. Phys.* **2015**, *48*, 145001.

[26] Girgis, E.; Wahsh, M. M.; Othman, A. G.; Bandhu, L.; Rao, K. *Nanoscale Res. Lett.* **2011**, *6*, 460.

[27] Pruthtikul, R.; Liewchirakorn, P. *JOM-J. Min. Mets.* **2008**, *18*, 63-66.

[28] Caizer, C.; Stefanescu, M, Muntean, C.; Hrianca, I. *Optoelectron. Adv. M.* **2001**, *3*, 919-924.

[29] Caizer, C.; Stefanescu, M. *J. Phys. D Appl. Phy.* **2002**, *35*, 3035-3040.

[30] Caizer, C.; Stefanescu, M. *Physica B* **2003**, *327*, 129-134.

[31] Elmasry, M.; Gaber, A. *J. Therm. Anal.* **1998**, *52*, 489-495.

[32] Kassabova-Zhetcheva, V.; Pavlova, L. *Journal of the University of Chemical Technology and Metallurgy* **2012**, *47*, 263-268.

[33] Maensiri, S.; Sangmanee, M.; Wiengmoon, A. *Nanoscale Res. Lett.* **2009**, *4*, 221-228.

[34] Krishnan, K.; Krishnan, R. S. *Proceedings of the Indian Academy of Science* **1966**, *64*, 111-122.

[35] Yang, J. *J. Xian Polytechnic Uni.* **2009**, *23*, 2.

[36] Gillot, B.; Jemmali, F.; Rousset, A. *J. Solid State Chem.* **1983**, *50*, 138.

[37] Ishii, M.; Nakahira, M.; Yamanaka, T. *Solid State Commun.* **1972**, *11*, 209.

[38] Wu, K. H.; Huang, W. C.; Wang, G. P.; Wu, T. R. *Mater. Res. Bull.* **2005**, *40*, 1822-1831.

[39] Pradeep, T. *A Textbook of Nanoscience and Nanotechnology*; Tata McGraw-Hill: New Delhi, India.

[40] Bhattacharjee, K.; Ghosh, C. K.; Mitra, M. K.; Das, G. C.; Mukherjee, S.; Chattopadhyay, K. K. *J. Nanopart. Res.* **2011**, *13*, 739-750.

[41] Abdeen, A. M. *J. Magn. Magm. Mater.* **1998**, *185*, 2199-2206.

[42] El Hiti, M. A. *J. Magn. Magm. Mater.* **1996**, *164*, 2187-2196.

[43] Sutka, A.; Mezinskis, G.; Lusis, A. *Phys. Scripta* **2013**, *87*, 2.

[44] Mathew, D. S.; Juang, R. S. *Chem. Eng. J.* **2007**, *129*, 51-65.

[45] Pradhan, D. K.; Misra, P.; Puli, V. S.; Sahoo, S.; Pradhan, D. K.; Katiyar, R. S. *J. Appl. Phys.* **2014**, *115*, 243904.

[46] Nandapure, A. I.; Kondawar, S. B.; Sawadh, P. S.; Nandapure, B. I. *Physica B* **2012**, *407*, 1104-1107.

[47] Ibrahim, E. M. M. *Appl. Phys. A* **2007**, *89*, 203-208.

[48] Verma, A.; Thakur, O. P.; Prakash, C.; Goel, T. C.; Mendiratta, R. G. *Mat. Sci. Eng. B-Adv.* **2005**, *116*, 1-6.

[49] El-Sayed, A. M. *Mater. Chem. Phys.* **2003**, *82*, 583-587.

[50] Sutka, K. *Sens. Lett.* **2013**, *11*, 2010-2013.

[51] Koops, C. G. *Phys. Rev.* **1951**, *83*, 121.

[52] Bhagwat, S.; Rao, P. *IOSR J. Applied Phys.* **2013**, *3*, 01-06.

[53] Ahmed, M. A.; El Zawawia, I. K.; Azab, A.; Almuhamady, A. *J. Am. Sci.* **2012**, *8*, 560-574.

[54] Pathan, A. T.; Shaik, A. M. *Int. J. Compt. Appl. T.* **2012**, *45*, 21.

[55] Raghavender, A. T.; Jadhav, K. M. *Bull. Mater. Sci.* **2009**, *32*, 575-578.

[56] Awati, V. V.; Bobade, D. H.; Kulkarni, S. D. *Int. J. Eng. Res. Appl.* **2012**, *2*, 482-489.